A Simple Theory for the Fate of Buoyant Coastal Discharges*

ALEXANDER E. YANKOVSKY AND DAVID C. CHAPMAN

Woods Hole Oceanographic Institution, Woods Hole, Massachusetts

ABSTRACT

A simple theory that predicts the vertical structure and offshore spreading of a localized buoyant inflow onto a continental shelf is formulated. The theory is based on two competing mechanisms that move the buoyant fluid offshore: 1) the radial spread of the lighter water over the ambient water, being deflected by the Coriolis force and producing an anticyclonic cyclostrophic plume, and 2) offshore transport of buoyant water in the frictional bottom boundary layer that moves the entire plume offshore while maintaining contact with the bottom. The surface expression of the cyclostrophic plume moves offshore a distance

$$y_s = 2(3g'h_0 + v_i^2)/(2g'h_0 + v_i^2)^{1/2}f,$$

where g' is reduced gravity based on the inflow density anomaly, h_0 is the inflow depth, v_i is the inflow velocity, and f is the Coriolis parameter. The plume remains attached to the bottom to a depth given by

$$h_b = (2Lv_ih_0f/g')^{1/2},$$

where L is the inflow width. Both scales are based solely on parameters of the buoyant inflow at its source.

There are three possible scenarios. 1) If the predicted h_b is shallower than the inflow depth, then the bottom boundary layer does not transport buoyancy offshore, and a purely *surface-advected plume* forms, which extends offshore a minimum of more than four Rossby radii. 2) If the h_b isobath is farther offshore than y_s, then transport in the bottom boundary layer dominates and a purely *bottom-advected plume* forms, which is trapped along the h_b isobath. 3) If the h_b isobath is deeper than the inflow depth but shoreward of y_s, then an intermediate plume forms in which the plume detaches from the bottom at h_b and spreads offshore at the surface to y_s.

The theory is tested using a primitive equation numerical model. All three plume types are reproduced with scales that agree well with the theory. The theory is compared to a number of observational examples. In all cases, the prediction of plume type is correct, and the length scales are consistent with the theory.

1. Introduction

Localized sources of buoyancy along the coastline represent one of the principal forcing mechanisms for coastal and shelf currents. These buoyant inflows on the shelf are typically associated with river discharges or exchanges between separate basins containing water masses of different density. As the buoyant inflow encounters the denser shelf water, a plume generally forms with a sharp density front separating the buoyant water from the shelf water. The structure of this plume may take a variety of shapes depending on the ambient flow, bottom topography, inflow properties, and wind forcing. However, most buoyant plumes may be categorized in terms of their contact with the bottom as follows.

In some cases, the plume occupies the entire water column into depths much greater than the depth of the inflow (Fig. 1). The accompanying coastal current remains in contact with the bottom well offshore, with the density front extending from the surface to the bottom. We refer to this plume as a *bottom-advected plume* because the behavior of the plume is basically controlled by advection in the bottom boundary layer (as discussed below). The flow on the Labrador Shelf may be viewed as an example of a bottom-advected plume. Cross-shelf sections of salinity and density (e.g., Figs. 3b,c and 15b from Lazier and Wright 1993) show that the buoyant flow spans the entire shelf with a frontal zone located near the shelf break. Thus, the offshore scale of this "plume" is more than 100 km, and the vertical scale (i.e., maximum depth attained) is about 200 m.

In other cases, a buoyant inflow primarily remains on top of the shelf water forming a thin layer with the ambient denser water beneath (Fig. 2). This plume may spread far offshore and has little contact with the bottom except perhaps very close to the coast. We call this a *surface-advected plume.* The discharge of the Niagara River into Lake Ontario is an example of a surface-

Corresponding author address: Dr. David C. Chapman, Physical Oceanography, Woods Hole Oceanographic Institution, Woods Hole, MA 02543.
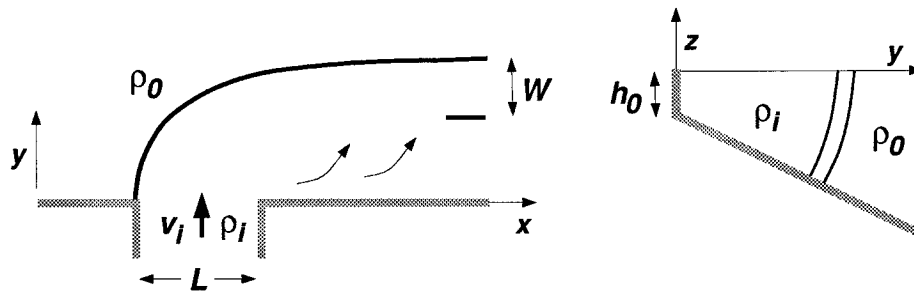E-mail: dchapman@whoi.edu

FIG. 1. Schematic of a bottom-advected plume.

advected plume in which the typical thickness of the buoyant layer is only 10 m (e.g., Fig. 7 from Masse and Murthy 1992). The plume spreads offshore about 10 to 15 km from the river mouth.

Of course, buoyant plumes may fall anywhere between the extremes of the bottom-advected plume and the surface-advected plume. These intermediate plumes occur when the buoyant flow spreads offshore, maintaining contact with the bottom for some distance beyond which the upper part of the plume detaches from the bottom and spreads seaward with the front between the ambient and buoyant waters gradually approaching the surface. Thus, the nearshore and near-bottom part of the plume has properties similiar to the bottom-advected plume, while the offshore and near-surface part behaves more like a surface-advected plume.

The list of theoretical or numerical studies considering the dynamics of buoyant plumes is quite long. Yet most of the papers deal with only one type of plume and do not discuss explicitly the transition from one type to the other. Several authors have acknowledged that offshore transport of buoyant water in the bottom boundary layer is a principal contributor to the cross-shelf movement of bottom-advected plumes (e.g., Csanady 1984; Wright 1989). Chapman and Lentz (1994) have shown that this effect moves the front offshore (over a sloping bottom) until it reaches the depth where the alongshelf velocity at the bottom within the front reverses, thus eliminating the offshore buoyancy flux in the bottom boundary layer. This reversal is caused by the vertical shear of the alongshelf velocity within the

front, which is in thermal wind balance with the density gradient across the front. Garvine (1996) considered a linear frictional model of the bottom-advected plume in which a steady state (isobath trapped) is achieved through the balance of bottom, interfacial, and wind stresses.

The dynamics of surface-advected plumes have attracted more attention than their bottom-advected counterparts. For example, Garvine (1987) and O'Donnell (1990) have shown that a surface buoyant inflow tends to spread radially from its source, being deflected to the right (in the Northern Hemisphere) by the Coriolis force and/or an ambient alongshelf current to form a surface-advected plume with anticyclonic circulation within the plume. Chao and Boicourt (1986), Chao (1988), Oey and Mellor (1993), and Kourafalou et al. (1996) have used numerical models to study idealized river discharges through estuaries, that, in most calculations, produce surface-advected plumes. The plume typically extends well offshore as a bulge that is attached to the estuary mouth and has anticyclonic flow within. In most cases, a substantially narrower buoyant coastal current appears adjacent to the coast, originating from the plume and propagating with the coast on its right.

The bottom-advected and surface-advected plumes appear to have very different dynamics, as reflected in the models used to study each one. Indeed, the two observational examples given above (Labrador Shelf and Niagara River) have remarkably different spatial scales and flow characteristics. On the other hand, there are also similarities. For example, the density difference
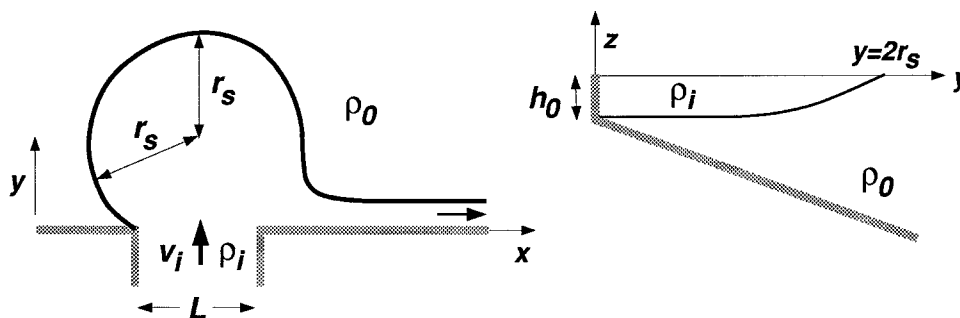

FIG. 2. Schematic of a surface-advected plume.

between the plume and the ambient flow is similar in both cases (approximately 1 kg m^{-3}), and the Coriolis force is important in both cases (both plume currents propagate with the coast on their right). So, we might expect that both types of plumes can be understood in terms of the same theoretical framework.

To develop a common theoretical framework, we use some rather simple ideas, based in part on previous studies, to derive two length scales that approximate the offshore expansion of the surface-advected and bottom-advected plumes (section 2). A comparison of these scales predicts which type of buoyant plume will form. The scales are based only on properties of the buoyant inflow at the source where it enters the shelf and on the shelf geometry, so the prediction of the offshore spread and plume type does not depend on any information about the buoyant flow after it enters the shelf. Then, to test the theory, a nonlinear, primitive equation, numerical model is used to simulate plumes formed by various idealized buoyant inflows (section 3). This is followed by the application of the theory to some observational examples (section 4). Finally, the results are briefly discussed and summarized (section 5).

2. Theory

Our goal is to predict which type of plume, bottom-advected or surface-advected, is produced by a specified buoyant inflow in the absence of complicating factors associated with the ambient shelf circulation. Therefore, the shelf waters are assumed initially quiescent (i.e., no mean flows or tides), and wind forcing is ignored. Furthermore, the details of the buoyant inflow within the estuary or river mouth are not considered. Instead, we assume that the plume is driven by a buoyant water discharge through a gap of width L in a coastal wall of depth h_0. The buoyant inflow has constant and spatially uniform velocity v_i and density anomaly ρ_i at the gap. Figures 1 and 2 depict these features for each plume type.

a. Bottom-advected plume

We begin by examining the bottom-advected plume (Fig. 1). We rely on the results of Chapman and Lentz (1994) for direction, although they did not derive the scales developed here. As the buoyant inflow enters the shelf, it is deflected to the right by the Coriolis force and propagates roughly parallel to the coast, remaining in contact with the bottom over virtually its entire extent. There may be a slow upstream spreading of buoyant water as well (e.g., Chapman and Lentz 1994; Kourafalou et al. 1996). However, its speed is much slower than the downstream flow, being easily suppressed by a weak cyclonic shelf current, which is typical for many shelves, so we ignore this feature in this section.

Based on the results of Chapman and Lentz (1994), we assume that the front along the offshore edge of the plume is established by offshore advection of buoyancy in the bottom boundary layer and that the front continues moving seaward until the alongshelf velocity within the front vanishes at the bottom. At this point the bottom boundary layer cannot move the front farther seaward. As the buoyant water shoreward of the front moves downstream, it is gradually forced offshore by the frictional bottom boundary layer in the same manner as described by Csanady (1978) for barotropic flow. This gradual offshore flow transports little buoyancy, but it eventually (i.e., far enough downstream) leads to the accumulation of the entire buoyant inflow transport within the frontal zone. (This tendency will be demonstrated in section 3.)

We can use this scenario to derive an expression for the equilibrium depth h_b, at which the bottom-advected plume becomes trapped. The transport within the frontal zone can be estimated by assuming uniform vertical shear of the alongfront velocity u, which is in thermal wind balance with the density gradient across the front. The transport at depth h_b within a front of width W is

$$T_b = \frac{1}{2} u_z h_b^2 W, \tag{1}$$

where the subscript z denotes partial differentiation, and $u = 0$ at the bottom, as described above. Thermal wind then provides an expression for the vertical shear as

$$u_z = g\rho_y/\rho_0 f \approx g'/fW, \tag{2}$$

where g is gravitational acceleration, ρ is the water density anomaly relative to a constant reference density ρ_0, $g' = g|\rho_i|/\rho_0$ is reduced gravity, and y is the offshore coordinate. Substituting (2) into (1) and then equating T_b to the inflow transport $Lv_i h_0$, in order to conserve mass, yields

$$h_b = (2Lv_i h_0 f/g')^{1/2}. \tag{3}$$

We can use h_b directly to locate the plume over any shelf topography, and this procedure is applied to the observational examples (section 4). For the numerical examples (section 3), however, the depth profile is chosen to be linearly increasing offshore as

$$h = h_0 + sy, \tag{4}$$

where s is the bottom slope, so we can easily estimate the offshore location of the bottom-advected plume y_b by finding the offshore distance to depth h_b:

$$y_b = \begin{cases} h_0[(2Lv_i f/g'h_0)^{1/2} - 1]/s, & h_b > h_0 \\ 0, & h_b < h_0. \end{cases} \tag{5}$$

It is important to recognize that y_b is positive only when $h_b > h_0$, that is, when the equilibrium depth is located somewhere offshore of the inflow isobath. Only then can the basic mechanism that forms the front and moves it offshore operate to create a bottom-advected plume. This tends to occur for strong inflows (large v_i) and/or weak density differences (small g'). In fact, h_b

and y_b increase without bound as $g' \to 0$. If the equilibrium depth is shallower than the coastal wall (i.e., shallower than the depth of the buoyant inflow), $h_b < h_0$, the bottom-advected plume cannot form, so we set $y_b = 0$.

b. Surface-advected plume

Figure 2 shows our version of an idealized surface-advected plume. We assume that the buoyant discharge forms an anticyclonic circulation with constant radius r_s and a narrow coastal current moving to the right. Within the anticyclone, we take the flow to be in steady, cyclostrophic balance, described by the following momentum equation:

$$-\hat{v}^2/r - f\hat{v} = -g'd_r, \tag{6}$$

where $\hat{v}$ is the azimuthal cyclostrophic velocity, d is the thickness of the buoyant layer, r is the radial distance from the center of the anticyclone, and the subscript r denotes partial differentiation. We also assume that the buoyant plume does not interact with the bottom, so its thickness is approximately uniform from the inflow to the center of the anticyclone and gradually decreases to zero along the outer edge. The radial change in plume thickness can then be approximated by $d_r = -h_0/r_s$, which allows (6) to be solved for r_s:

$$r_s = -\frac{g'h_0 + \hat{v}_s^2}{f\hat{v}_s}, \tag{7}$$

where $\hat{v}_s$ is the azimuthal velocity at the edge of the plume (i.e., at radius r_s). Since r_s must be positive, the minus sign means that $\hat{v}_s$ must be negative, indicating anticyclonic flow.

To obtain an estimate for $\hat{v}_s$, we consider the Bernoulli function for the buoyant layer, defined following Gill (1982), as

$$B = g'd + \hat{v}^2/2, \tag{8}$$

which is constant along a streamline (in the absence of diffusive processes). Taking the outer edge of the plume to be a streamline connected to the inflow, then B along the outer edge of the plume must be equal to B at the inflow. Evaluating B at the two locations and equating (and noting that $d = 0$ along the outer edge of the plume) yields

$$g'h_0 + v_i^2/2 = \hat{v}_s^2/2,$$

which can be rewritten as

$$\hat{v}_s = -(2g'h_0 + v_i^2)^{1/2}, \tag{9}$$

where the minus sign corresponds to anticyclonic flow.

Substituting (9) into (7), we obtain an estimate for the maximum seaward expansion of the surface-advected plume, based only on the inflow properties,

$$y_s = 2r_s = \frac{2(3g'h_0 + v_i^2)}{f(2g'h_0 + v_i^2)^{1/2}} = R_{di}\frac{2(3 + F_i^2)}{(2 + F_i^2)^{1/2}}, \tag{10}$$

where $R_{di} = (g'h_0)^{1/2}/f$ may be referred to as the baroclinic Rossby radius of the buoyant inflow, and $F_i = v_i/(g'h_0)^{1/2}$ is the inflow Froude number. It is interesting to consider two limits of (10). First, a weak buoyant inflow or large density difference (i.e., $v_i^2 \ll g'h_0$; $F_i \ll 1$) yields $y_s = 4.24R_{di}$. That is, the surface-advected plume spreads a minimum of more than four inflow Rossby radii offshore. This result is in good agreement with the study of Oey and Mellor (1993). In their model, $h_0 = 10$ m and the density difference between the inflow and the ambient water is approximately 20 kg m^{-3} (see their Fig. 2), producing $R_{di} = 14$ km and a minimum offshore expansion of $y_s = 60$ km [taking $v_i \to 0$ or $F_i \to 0$ in (10)], which is consistent with their model result. Second, in the limit of strong inflow or small density difference (i.e., $v_i^2 \gg g'h_0$; $F_i \gg 1$), then $y_s = 2v_i/f$, and the inflow turns in an inertial circle.

c. Interpretations

We can use the length scales h_b and y_s to predict which dynamics should dominate and how the buoyant inflow should behave, based only on the inflow parameters. Our reasoning is as follows. Transport in the bottom boundary layer can move the buoyant inflow offshore to depth h_b. Surface processes can carry the buoyant inflow a distance y_s offshore. The location of the h_b isobath (y_b for a linear bottom slope) relative to y_s determines the plume behavior. There are three possible outcomes:

1) $h_b < h_0$ ($y_b = 0$): The predicted equilibrium depth for the bottom-advected plume is shallower than the depth of the buoyant inflow, so bottom boundary layer dynamics have no influence. A surface-advected plume forms.

2) $h_b > h_0$, and h_b is shoreward of y_s ($0 < y_b < y_s$): An intermediate plume forms in which the front detaches from the bottom approximately at depth h_b and extends offshore at the surface to y_s, like a surface-advected plume.

3) $h_b > h_0$, and h_b is offshore of y_s ($y_b > y_s$): Bottom boundary layer transport moves the front farther offshore than surface processes can. A bottom-advected plume forms.

Additional insight may be gained by casting the theory in terms of nondimensional parameters, which also simplifies the interpretation somewhat. We define a Burger number S and a Rossby number Ro in terms of the inflow parameters as

$$S = (g'h_0)^{1/2}/fL; \quad \text{Ro} = v_i/fL. \tag{11}$$

The Burger number is a measure of the influence of buoyancy, while the Rossby number is a measure of the nonlinear advection of momentum (or rate of inflow) through the coastal gap. (We could have chosen to use the inflow Froude number, $F_i = \text{Ro}/S$, in place of either S or Ro in what follows. However, S and Ro allow the
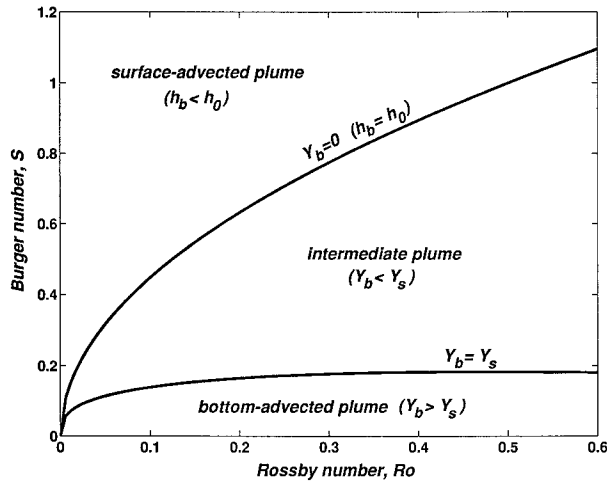
FIG. 3. Regions of various plume types based on the theory of section 2 with $h_0/sL = 0.278$.

FIG. 4. Model domain for the numerical calculations in section 3.

separation of buoyancy and nonlinear effects, which we find helpful.) The horizontal lengths y_b and y_s are then scaled by L, so that (5) and (10) can be written as

$$Y_b = \frac{h_0}{sL}\left(\frac{(2\mathrm{Ro})^{1/2}}{S} - 1\right) \tag{12}$$

$$Y_s = \frac{2(3S^2 + \mathrm{Ro}^2)}{(2S^2 + \mathrm{Ro}^2)^{1/2}}, \tag{13}$$

where Y_b and Y_s are the scaled equivalents of y_b and y_s, respectively.

There are now three nondimensional parameters that define the plume behavior: S, Ro, and a geometrical parameter h_0/sL. Figure 3 shows the three plume regimes listed above in terms of S versus Ro for a fixed geometrical parameter $h_0/sL = 0.278$ ($h_0 = 25$ m, $s = 3 \times 10^{-3}$, $L = 30$ km, all of which are used in our numerical calculations). The upper curve corresponds to $Y_b = 0$ in (12), which is equivalent to setting $h_b = h_0$. This curve is independent of h_0/sL, and represents the division between surface-advected plumes and intermediate plumes. Any combination of S and Ro lying above this curve, that is, $S > (2\,\mathrm{Ro})^{1/2}$, should produce a surface-advected plume, regardless of the shelf topography (provided the depth increases offshore). The lower curve in Fig. 3 corresponds to $Y_b = Y_s$ (or equivalently $y_b = y_s$) and represents the division between intermediate plumes and bottom-advected plumes. Any combination of S and Ro lying below this curve should produce a bottom-advected plume. The location of the lower curve depends on the geometrical parameter h_0/sL; the curve moves toward higher S at each Ro when h_0/sL increases. That is, the intermediate region in Fig. 3 shrinks as h_0/sL increases (the upper curve is unaffected).

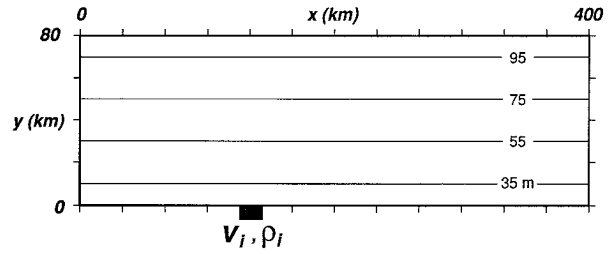It is important to note that the lower curve in Fig. 3 has a local maximum S as a function of Ro, which means

that a pure bottom-advected plume is possible only for a relatively weak density difference between the ambient flow and buoyant discharge (small S). When the density difference is large enough that S exceeds this maximum, then either an intermediate or a surface-advected plume will be established no matter how strong the inflow velocity may be (i.e., independent of Ro). This also means that a surface-advected plume is more likely to occur at lower latitudes than a bottom-advected plume because f decreases, making S larger (all else remaining equal).

3. Numerical calculations

a. Model description

We use the semispectral primitive equation model (SPEM), described by Haidvogel et al. (1991), to test the theory of the previous section. The momentum balance is based on the hydrostatic and Boussinesq approximations and may be written, along with the continuity and density equations, in the following form:

$$u_t + \mathbf{v}\cdot\nabla u - fv = -\frac{1}{\rho_0}p_x + A_H\nabla_\sigma^2 u + (A_V u_z)_z \tag{14}$$

$$v_t + \mathbf{v}\cdot\nabla v + fu = -\frac{1}{\rho_0}p_y + A_H\nabla_\sigma^2 v + (A_V v_z)_z \tag{15}$$

$$p_z = -g\rho \tag{16}$$

$$u_x + v_y + w_z = 0 \tag{17}$$

$$\rho_t + \mathbf{v}\cdot\nabla\rho = K_H\nabla_\sigma^2\rho + (K_V\rho_z)_z. \tag{18}$$

In this system (u, v, w) are the (x, y, z) components of the velocity vector $\mathbf{v}$, p is the pressure, ρ is the density difference from a constant reference density $\rho_0 = 1010$ kg m^{-3}, f is the Coriolis parameter, and g is gravitational acceleration. Here A_H and A_V are lateral and vertical viscosities, respectively, and K_H and K_V are lateral and vertical diffusivities. Lateral Laplacian mixing and diffusion ∇_σ^2 are applied along σ-coordinate surfaces. Subscripts t, x, y, z denote partial differentiation with respect to time and the spatial coordinates.

The numerical domain is a straight channel (Fig. 4) with a coastal wall of depth $h_0 = 25$ m at $y = 0$ and a solid wall offshore at $y = 80$ km. The channel length is 400 km. The cross-channel boundaries at $x = 0$ and

$x = 400$ km are discussed below. The depth increases linearly away from the coast as given by (4) with the slope s chosen in the range 0.001–0.003. The channel is uniformly rotating with $f = 10^{-4}$ s^{-1}. The numerical grid is rectangular and uniform in the horizontal with 161 along-channel and 65 cross-channel grid points (i.e., $\Delta x = 2.5$ km and $\Delta y = 1.25$ km). Nine Chebyshev polynomials are used to resolve the vertical structure. The model time step is 240 s.

The boundary conditions are as follows. A rigid lid is assumed at the surface ($w = 0$ at $z = 0$). No flow is permitted through the bottom or the side walls except for a localized buoyancy inflow through a gap in the coastal wall usually between $x = 60$ km and $x = 90$ km, that is, $L = 30$ km. There is no stress at the surface or at the sidewalls. The shear stress at the bottom is specified using a linear bottom friction parameterization,

$$A_V u_z = ru; \quad A_V v_z = rvz = -h, \qquad (19)$$

where the bottom friction coefficient is set to $r = 0.0005$ m s^{-1}. The vertical viscosity and diffusivity are fixed at $A_V = K_V = 0.001$ m^2 s^{-1} for cases involving bottom-advected plumes. However, for calculations strongly influenced by surface-advected plumes, constant vertical mixing coefficients tend to smear the frontal region. So, for these cases, we employ a parameterization that sets the viscosity and diffusivity based on the local Richardson number:

$$A_V = 0.0001 + \frac{0.0009}{(1. + 0.3\text{Ri})^{1/2}}$$

$$K_V = 0.0001 + \frac{0.0009}{(1. + 0.3\text{Ri})^{3/2}},$$

where the units are m^2 s^{-1} and the Richardson number is defined by

$$\text{Ri} = \frac{-g\rho_z/\rho_0}{(u_z)^2 + (v_z)^2}.$$

The maximum value for A_V and K_V is still 0.001 m^2 s^{-1}. We choose the smallest coefficients of lateral mixing that provide stable numerical calculations; $A_H = 50$ m^2 s^{-1} and $K_H = 10$ m^2 s^{-1}.

There are no density fluxes through the bottom, surface, and side walls except for the specified buoyant inflow through the coastal gap, which enters the model domain with uniform velocity v_i and density anomaly ρ_i.

At the upstream boundary ($x = 0$), we specify a uniform inflow with $u = 0.04$ m s^{-1} and $\rho = 0$. The purpose of this weak barotropic mean current is to prevent the plume from propagating upstream. At the downstream boundary we use the open boundary condition of Chapman and Lentz (1994) in which the vorticity and depth-averaged velocity components are advected out with a radiation condition, and a zero-gradient condition is applied to the depth-varying quantities. This boundary condition works quite well for the mean component of the frontal velocity field, which basically has a two-dimensional (y–z) structure downstream from the buoyancy source. In addition, we apply a sponge layer over the last 50 km of the model domain on the baroclinic part of v. This does not alter the frontal structure but effectively suppresses any transient features appearing due to the initial adjustment of the buoyant inflow or due to instabilities of the frontal current.

Each model run begins with water of constant density $\rho = 0$ flowing at constant velocity (0.04 m s^{-1}) with the coast on its right. The buoyant inflow is imposed and is held constant until the buoyant plume within the model domain reaches an approximate steady state. Although true steady-state dynamics have not been achieved in some calculations, the plume always evolves long enough to distinguish its behavior in terms of our simple theory.

b. Results

The purpose of the numerical calculations is to demonstrate the validity of our theory for the case of fully nonlinear dynamics (at least in the range of parameters considered). In fact, the scales derived in section 2 not only correctly predict plume type, but also provide a fairly accurate estimate of the offshore extent of the plume.

We vary four model parameters within the following ranges: velocity of the buoyant inflow, $0.1 < v_i < 0.5$ m s^{-1}, density anomaly of the buoyant inflow, $-2.5 < \rho_i < -0.5$ kg m^{-3}, width of the coastal gap, $20 < L < 30$ km and bottom slope, $0.001 < s < 0.003$. The inflow (coastal) depth is fixed at $h_0 = 25$ m. The linear bottom slope conveniently allows us to categorize the behavior entirely in terms of y_b and y_s, because y_b is a known function of h_b. Variations in v_i and ρ_i affect both y_b and y_s, but variations in L and s modify only y_b. Table 1 summarizes the model calculations and presents the predicted lengths y_s, y_b, and h_b.

1) BOTTOM-ADVECTED PLUMES: $y_b > y_s$

The first four model calculations are cases in which a bottom-advected plume should form, according to the theory (i.e., $y_b > y_s$). Run 1 provides a good example of the bottom-advected plume, with the predicted offshore location $y_b = 30.6$ km compared to $y_s = 21.2$ km. In fact, this run repeats the standard case from Chapman and Lentz (1994) with two differences: (i) the plume does not move upstream because of the presence of the imposed mean along-channel current and (ii) the nonlinear momentum balance allows instabilities in the frontal current.

Figure 5 shows plan views of the depth-averaged (or barotropic) streamfunction, surface velocity vectors, and surface density anomaly on day 90. Figure 6 shows cross-shelf sections of u, v, and ρ at $x = 200$ km (i.e.,

TABLE 1. Parameters for the numerical calculations discussed in section 3. Runs 1–4 form bottom-advected plumes. Run 5 forms a surface-advected plume. Runs 6–9 form intermediate plumes. Variables are defined in the text except for x_u, which is the along-shelf coordinate of the upstream edge of the buoyant inflow. Units are kilometers for x_u, L, y_s, and y_b; meters per second for v_i; kilograms per cubic meter for ρ_i; and meters for h_b. In each case, the coastal depth is $h_0 = 25$ m. Runs 5–9 use the variable vertical mixing coefficients defined in section 3.

Run	x_u	L	s	v_i	ρ_i	Ro	S	h_0/sL	y_s	h_b	y_b
1	60	30	0.001	0.2	−1.0	0.067	0.164	0.833	21.2	55.6	30.6
2	60	30	0.001	0.3	−1.0	0.100	0.164	0.833	21.6	68.1	43.1
3	60	30	0.003	0.3	−0.5	0.100	0.116	0.278	15.7	96.3	23.8
4	60	30	0.003	0.5	−0.5	0.167	0.116	0.278	17.5	124.3	33.1
5	90	20	0.003	0.15	−2.5	0.075	0.389	0.417	33.1	24.9	0.0
6	60	30	0.003	0.3	−1.0	0.100	0.164	0.278	21.6	68.1	14.4
7	60	30	0.003	0.2	−1.0	0.067	0.164	0.278	21.2	55.6	10.2
8	60	30	0.003	0.3	−2.0	0.100	0.232	0.278	30.0	48.2	7.7
9	90	30	0.003	0.2	−2.5	0.067	0.260	0.278	33.2	35.2	3.4

110 km downstream of the buoyancy source). In general, the plume develops according to our expectations. It turns to the right as it enters the model domain, occupying the entire water column, and gradually spreads offshore to a distance of about 30 km as predicted. The downstream convergence of streamfunction contours near the offshore edge of the plume (Fig. 5a) demonstrates that the flow gradually accumulates within the frontal zone as the buoyant current flows downstream. A fairly long alongshelf distance is required for the total transport of buoyant inflow to be confined within the frontal zone. However, the velocities shoreward of the front at the downstream end of the model domain ($x = 300$–350 km in Fig. 5b) are quite small, showing that the flow assumed in deriving y_b (section 2) has almost been established.

Figure 6a shows that the frontal zone has moved offshore to the depth where u reverses at the bottom of the front, thereby eliminating offshore buoyancy transport in the bottom boundary layer within the entire frontal zone. At this downstream location, the frontal current is still stable (instabilities appear farther downstream
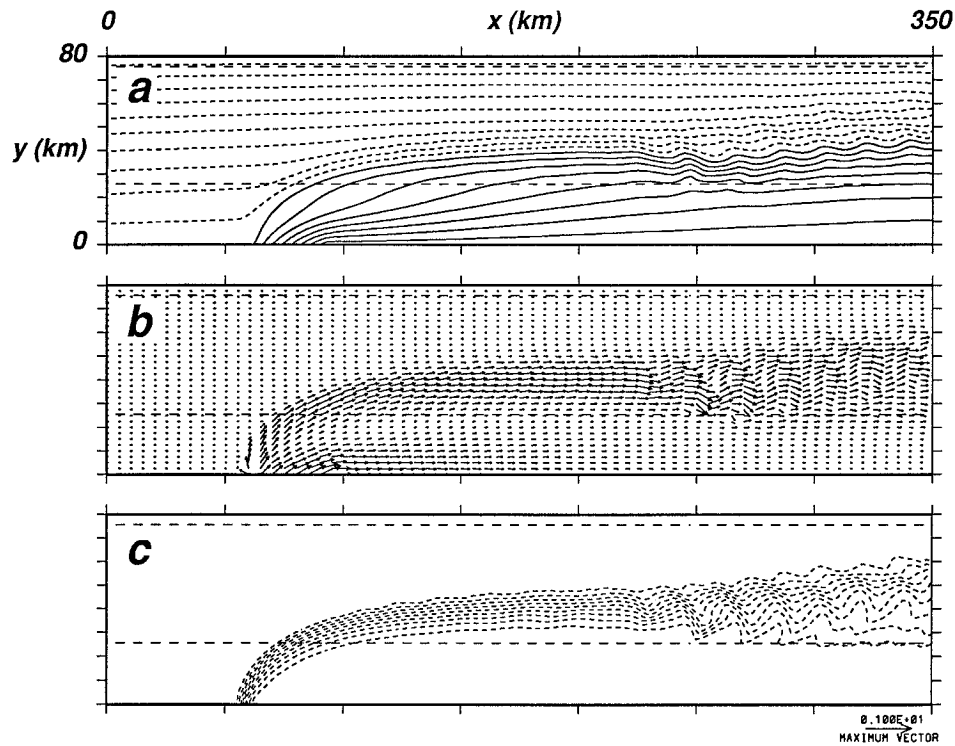

FIG. 5. Plan views of (a) streamfunction, (b) surface velocity vectors (plotted every second grid point), and (c) density anomaly at the surface for run 1 (Table 1) at day 90. Contours are -1.9×10^5 to 1.5×10^5 by 2×10^4 m³ s⁻¹ for streamfunction and $0.1\rho_i$ to $0.9\rho_i$ by $0.1\rho_i$ kg m⁻³ for density anomaly. Negative contours are dashed and positive contours are solid. The straight dashed lines are the 50-m and 100-m isobaths.

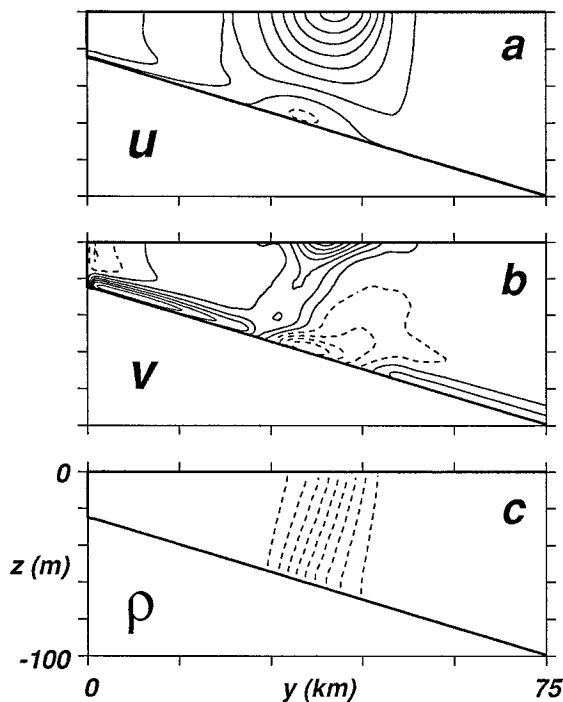FIG. 6. Cross-shelf sections of (a) alongshelf velocity u, (b) cross-shelf velocity v, and (c) density anomaly ρ at $x = 200$ km for run 1 (Table 1) at day 90. Contours are -0.02 to 0.30 by 0.04 m s^{-1} for u, -0.0175 to 0.0325 by 0.005 m s^{-1} for v, $0.1\rho_i$ to $0.9\rho_i$ by $0.1\rho_i$ kg m^{-3} for ρ. Negative contours are dashed and positive contours are solid.

and are discussed below). The vertical shear of u within the frontal zone is almost linear, in agreement with our assumption in section 2. Across the base of the front (i.e., where the frontal zone contacts the bottom), bottom boundary layer transport is everywhere toward the coast (Fig. 6b). The shoreward edge of the frontal zone is trapped approximately 30 km from the coast (Fig. 6c), which is in good agreement with y_b (Table 1).

Model runs 2–4 (Table 1) are cases in which various parameters have been changed from those in run 1, but a bottom-advected plume is both predicted and formed in each case. The resulting streamfunction and surface density fields are shown in Figs. 7 and 8, respectively. The basic behavior is identical to that described above for run 1 (Figs. 5 and 6), but there are several revealing differences in the details.

Run 2 (Figs. 7a and 8a) is identical to run 1 except that the inflow velocity is greater ($v_i = 0.3$ m s^{-1}). This increases the inflow transport of buoyant water and thereby moves the frontal zone farther offshore according to (5); $y_b = 43.1$ km. The frontal instabilities arise closer to the inflow, and the plume needs a longer alongshelf distance to reach the equilibrium depth. A substantial part of the buoyant transport is still carried between the coast and the frontal zone at the downstream edge of the model domain.

Increased bottom slope s reduces y_b (i.e., the equilib-

rium depth occurs closer to the coast) but does not change y_s. Run 3 (Figs. 7b and 8b) and run 4 (Figs. 7c and 8c) use a steeper bottom slope $s = 0.003$, but a smaller inflow density anomaly $\rho_i = -0.5$ kg m^{-3} in order to ensure a bottom-advected plume. In both cases, the plume is confined closer to the coast than in the previous examples, but a longer alongshelf distance is required for the transport to be confined to the frontal zone. For run 3, the frontal zone is narrower and the instabilities appear only near the downstream boundary. The flow shoreward of the front can be seen converging slowly toward the front, with the edge of the front at the downstream boundary located at $y = 23$–25 km, close to the estimate of $y_b = 23.8$ km.

Run 4 has the greatest inflow transport ($v_i = 0.5$ m s^{-1}) and, as a result, requires an extremely long along-shelf distance for the transport to be confined within the frontal zone. In fact, streamfunction contours at the downstream boundary are almost equally spaced, and the velocity at the coast matchs (if not exceeds) the maximum velocity within the frontal zone (not shown). Neither density nor streamfunction contours are parallel to the coast at the downstream boundary. Nevertheless, the flow is moving gradually offshore and would eventually collect at h_b to produce a bottom-advected plume.

The instabilities along the frontal current (i.e., smaller-scale wiggles), which appear in Figs. 5, 7, and 8, deserve some discussion, although a thorough analysis is beyond the scope of this paper. In particular, the onset of the instabilities appears to have a simple explanation. The instabilities appear early in the model calculations, after about 20–25 days, and they are clearly frontally trapped (i.e., they decay both seaward and shoreward away from the frontal zone). They presumably grow due to both vertical and horizontal shear (i.e., they have both vertical and horizontal structure), but the horizontal shear apparently acts as a trigger for their development. To demonstrate, remember that a necessary condition for a purely barotropic along-isobath current to be unstable is that the cross-current derivative of the background potential vorticity, $P = (f - U_y)/h$, must change sign (here U is the barotropic mean current velocity; see Collings and Grimshaw 1980 for more details). We can estimate U from the streamfunction field as $U = -\psi_y/h$ and calculate P across the channel at any x. As the flow accumulates in the frontal zone (i.e., stream-function contours converge), the horizontal shear of the current within the frontal zone increases. Figure 9 shows estimates of P from run 1 at $x = 160$ and 200 km at day 25, when the instabilities begin to appear. Upstream of the instabilities, at $x = 160$ km, P decreases monotonically offshore. However, at the point where the instabilities first appear, P_y changes sign across the front. For a stronger inflow (run 2, Fig. 7a) the frontal current shear reaches the point where P_y changes sign closer to the source, and the instabilities appear near $x = 150$ km. For runs 3 and 4 (Figs. 7b,c), the shear of the frontal current is rather weak throughout nearly the entire mod-
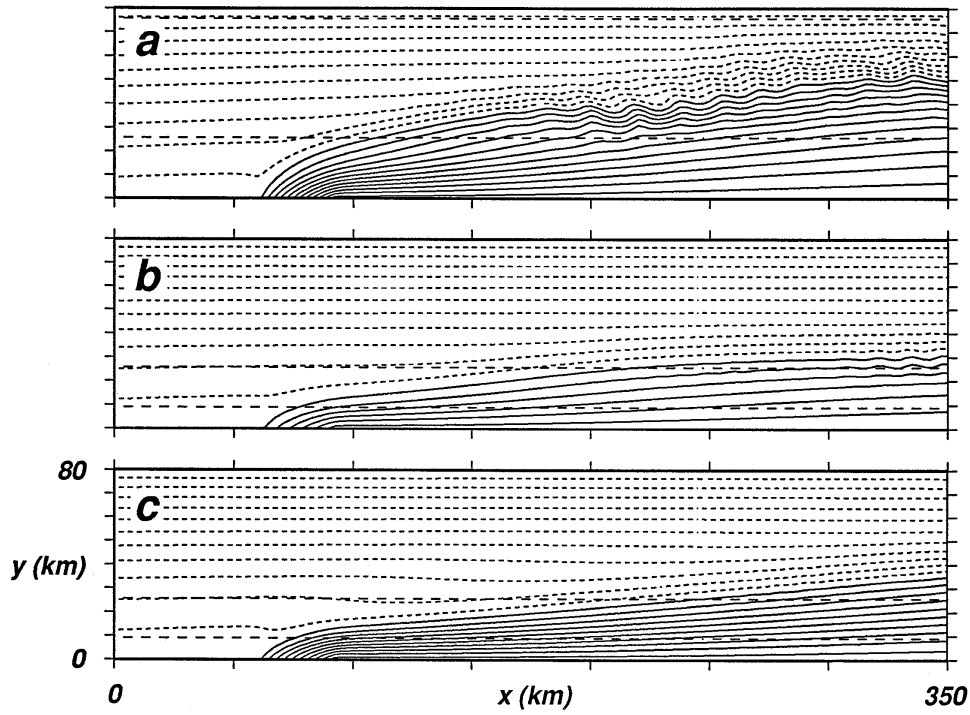
FIG. 7. Plan views of streamfunction for (a) run 2 at day 90, (b) run 3 at day 60, and (c) run 4 at day 90. Contours are -1.9×10^5 to 2.3×10^5 by 2×10^4 m^3 s^{-1} in (a); -4.2×10^5 to 2.2×10^5 by 4×10^4 m^3 s^{-1} in (b); -4.2×10^5 to 3.8×10^5 by 4×10^4 m^3 s^{-1} in (c). The straight dashed lines are the 50-m and 100-m isobaths.
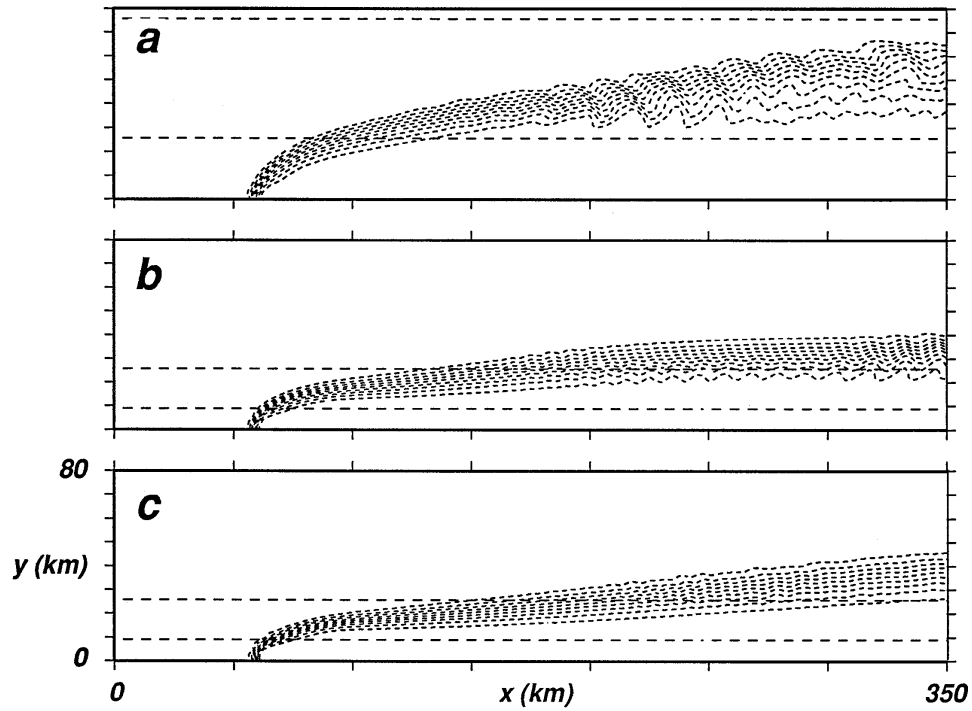
FIG. 8. As in Fig. 7 but plan views of density anomaly at the surface. Contours are $0.1\rho_i$ to $0.9\rho_i$ by $0.1\rho_i$ kg m^{-3}.
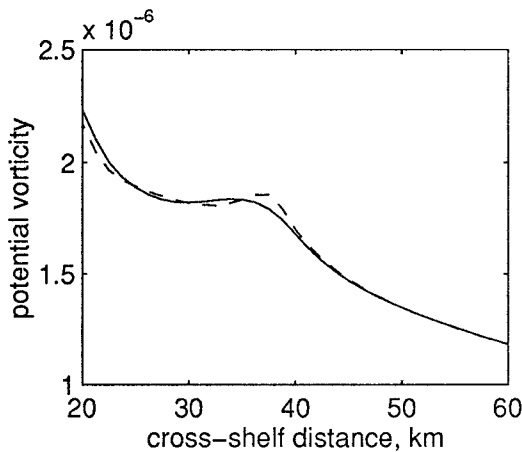
FIG. 9. Cross-shelf profiles of potential vorticity P at $x = 160$ km (solid line) and $x = 200$ km (dashed line) for run 1, day 25.

el domain. Instabilities barely appear in run 3 and do not appear in run 4. A more thorough investigation shows that, in every case we have computed, the instabilities start to grow precisely where P_y first has a sign change across the frontal current. Furthermore, the instabilities tend to disappear some distance downstream apparently because the flow associated with the instabilities causes widening of the front and, therefore, weakening of the frontal shear such that P_y no longer

changes sign across the front. Although this analysis does not prove that the wiggles are generated by barotropic instability, it strongly supports that contention.

2) SURFACE-ADVECTED PLUMES: $y_b = 0$

Run 5 (Table 1) is an example of a surface-advected plume; $y_b = 0$. In this case, $h_b = 24.9$ m, which is slightly smaller than $h_0 = 25$ m. By day 25, the buoyant inflow forms a plume with anticyclonic circulation spreading from the source and an outgoing narrower buoyant current attached to the coastal wall (Fig. 10). The outermost streamfunction contour of the "cyclostrophic" plume has a maximum offshore extent remarkably close to $y_s = 33.1$ km. Cross-shelf sections of the plume at $x = 130$ and 250 km (Fig. 11) show that u is zero or negative at the bottom everywhere (Figs. 11a,c), confirming that $h_b < h_0$, so bottom boundary layer transport cannot move the front offshore. The core of the plume (i.e., water with the inflow density) does not contact the sloping bottom (Figs. 11b,d).

The structure of the surface-advected plume shown in Figs. 10 and 11 is similar to the plume reported by Oey and Mellor (1993). However, in our case the buoyant inflow is in full contact with the sloping frictional bottom when entering the model domain, and we have imposed a weak alongshelf current at $x = 0$. Both of these features conspire to produce a somewhat elongated
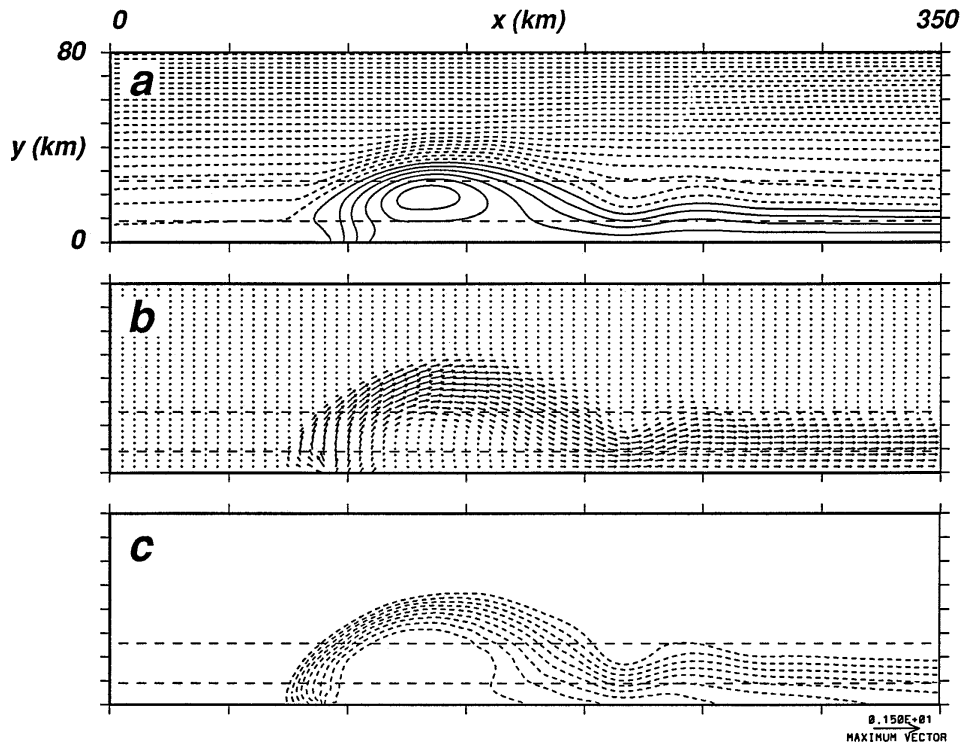

FIG. 10. As in Fig. 5 but for run 5, day 25. Contours are -4.5×10^5 to 1.1×10^5 by 2×10^4 m^3 s^{-1} for streamfunction and $0.1\rho_i$ to $0.9\rho_i$ by $0.1\rho_i$ kg m^{-3} for density anomaly. Negative contours are dashed and positive contours are solid.
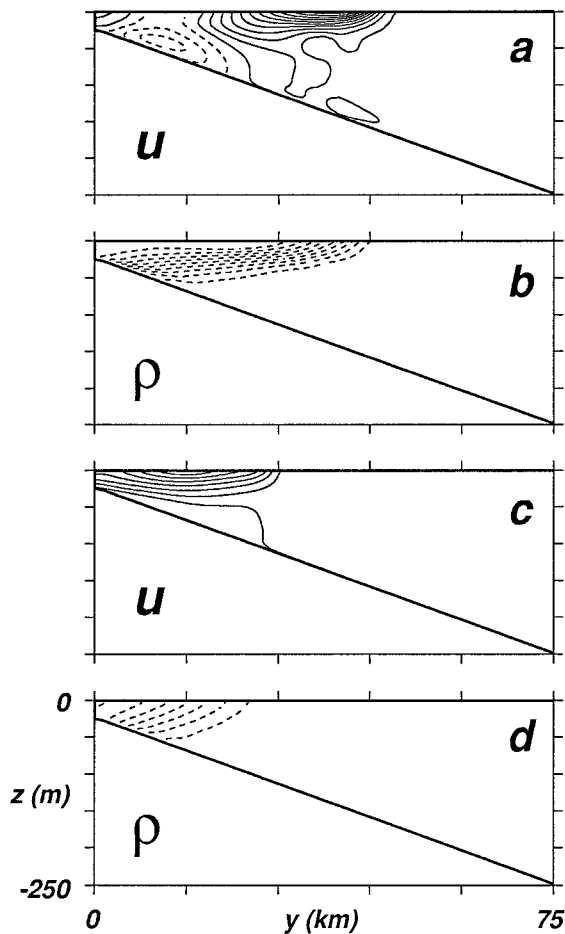
FIG. 11. Cross-shelf section of (a) alongshelf velocity u and (b) density anomaly ρ at $x = 130$ km, and (c) alongshelf velocity u and (d) density anomaly ρ at $x = 250$ km for run 5 (Fig. 10) at day 25. Contours are -0.10 to 0.42 by 0.04 m s^{-1} in (a); and -2.25 to -0.25 by 0.25 kg m^{-3} in (b); 0.02 to 0.26 by 0.04 m s^{-1} in (c); and -1.75 to -0.25 by 0.25 kg m^{-3} in (d). Negative contours are dashed and positive contours are solid.

(not precisely circular) anticyclone. Nevertheless, our plume looks remarkably like the model of Garvine (1987), including the narrowing of the front where the anticyclone reattaches to the coast ($x \approx 220$ km in Fig. 10). There the model appears to develop a flow qualitatively akin to the coastal front described by Garvine (1987; e.g., his Fig. 15). Of course, the present model is too diffusive to generate extremely sharp discontinuities.

3) INTERMEDIATE PLUMES: $0 < y_b < y_s$

Model runs 6–9 (Table 1) correspond to intermediate buoyant plumes that have properties of both the bottom-advected and surface-advected plumes. The structure of these intermediate plumes depends on the relative sizes of y_s and y_b. Basically, the base of the plume (where it attaches to the bottom) moves offshore to y_b, while the

surface expression of the plume moves offshore to y_s. If y_s only slightly exceeds y_b, then the plume is almost a bottom-advected plume. If y_s is much larger than y_b, then the plume is almost a surface-advected plume. In other words, the proximity of the parameters to the two curves in Fig. 3 determines the structure of the resulting plume.

Figures 12 and 13 show the streamfunction and surface density fields for the intermediate plumes, with the ratio y_s/y_b ranging from 1.5 to 9.8 (Table 1). These examples essentially span the transition from nearly bottom-advected plumes to nearly surface-advected plumes. In each case, the intermediate plume has characteristics of both the bottom-advected and surface-advected plumes. At the surface, the inflow near the buoyancy source moves offshore close to y_s, like the surface-advected plume (Fig. 10). Some of the inflow moves more directly toward the right, forming a frontal zone downstream that is parallel to the coast close to y_b and in which the transport accumulates, like the bottom-advected plumes (Figs. 5, 7, and 8).

The relevance of the lengths y_s and y_b is most clearly seen in cross-shelf sections of density anomaly (Fig. 14), which show the intersection of the frontal zone with both surface and bottom. These sections correspond to each of the intermediate cases shown in Figs. 12 and 13. In each case, the shoreward edge of the frontal zone intersects the bottom and the surface remarkably close to the estimates y_b and y_s, respectively. This provides strong support for the theory presented in section 2.

We have made numerous additional calculations, with many different combinations of parameters. We do not show any more results because they are all consistent with the results presented thus far and with the theory of section 2. In all cases, the buoyant discharge behaves according to the three regimes in Fig. 3 with a smooth transition from bottom-advected plumes to surface-advected plumes as depicted in Figs. 12, 13, and 14. We have yet to find an exception.

4. Observational examples

In this section we apply our simple theory to several observational examples that are documented well enough to obtain all the necessary information. Estimates of y_s and h_b are based on the buoyant inflow parameters at the mouth. We then estimate y_b based on the actual shelf topography to avoid approximating an average bottom slope. That this information is typically available is an advantage of our theory. However, we still need the appropriate observations of buoyant plumes on the shelves to compare the theoretical prediction with reality. Table 2 summarizes the observational examples considered in this section.

We start with the two examples mentioned in the introduction. Cases 1 and 2 represent the Niagara River plume. Here the density anomaly is caused by the temperature difference between the warmer Niagara River
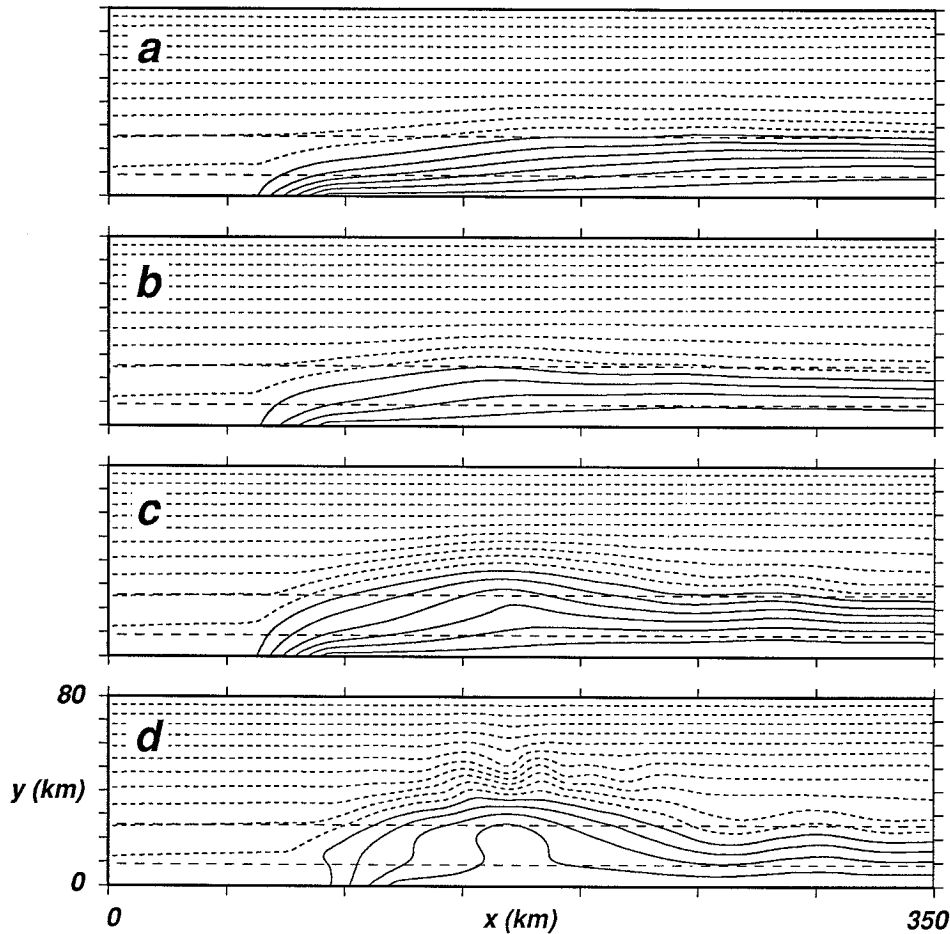
FIG. 12. Plan views of streamfunction for (a) run 6, (b) run 7, (c) run 8, and (d) run 9 each at day 30. Contours are -4.2×10^5 to 2.2×10^5 by 4×10^4 m^3 s^{-1} in (a); -4.2×10^5 to 1.4×10^5 by 4×10^4 m^3 s^{-1} in (b); -4.2×10^5 to 2.2×10^5 by 4×10^4 m^3 s^{-1} in (c); and -4.2×10^5 to 1.4×10^5 by 4×10^4 m^3 s^{-1} in (d). The straight dashed lines are the 50-m and 100-m isobaths.

and colder Lake Ontario. Masse and Murthy (1992) show that the typical density difference for the summer is in the range 0.5–1.0 kg m^{-3}. Thus, the first estimate (case 1) corresponds to the lower limit (0.5 kg m^{-3}, Table 2). In case 2 we are more specific and consider the density difference of approximately 0.9 kg m^{-3} observed on 17 July 1984. The temperature of the plume was 21.5°C, while the temperature of the ambient flow was 17°C. The river mouth width is 1.5 km, and $h_0 = 10$ m. The buoyant inflow occupies the mouth from surface to bottom. The inflow velocity estimate is based on the typical rate of Niagara River discharge, which is 6500 m^3 s^{-1}, giving $v_i = 0.4$ m s^{-1}.

For the first case (Niagara 1), the discharge should form an intermediate plume according to our theory. The attachment depth for the bottom-advected plume is $h_b = 15.6$ m, which corresponds to $y_b \approx 5$ km based on the local topography near the mouth. The offshore extent of the surface-advected plume should be $y_s = 12.2$ km. For the second case (Niagara 2), $h_b = 11.6$ m, which is close to h_0, suggesting that the discharge

should form a nearly surface-advected plume. Masse and Murthy (1992; their Fig. 7b) show a cross-shelf section at the Niagara River mouth from 17 July 1984 in which the plume detaches from the bottom at a depth of 12–13 m ($h_b = 11.6$ m). A plan view of the plume on the same day (their Fig. 6) shows that the 19°C isotherm (representing the average location of the frontal zone) extends 11–12 km offshore ($y_s = 14.8$ km). Thus, our estimates are close in predicting the observed discharge behavior.

Information about the buoyant inflow driving the Labrador Shelf current is less certain. We assume that the principal buoyant source for the fresher Labrador Shelf water is the flow exiting Hudson Strait along the southern coast. We use the work of Drinkwater (1988; his Fig. 3 and Table 1) to obtain the necessary parameters. The density of the current flowing along the Quebec coast gradually changes from its core to its periphery without any sharp boundary. Therefore, we choose two cases for the buoyant inflow onto the Labrador Shelf through the mouth of Hudson Strait. The first (Labrador
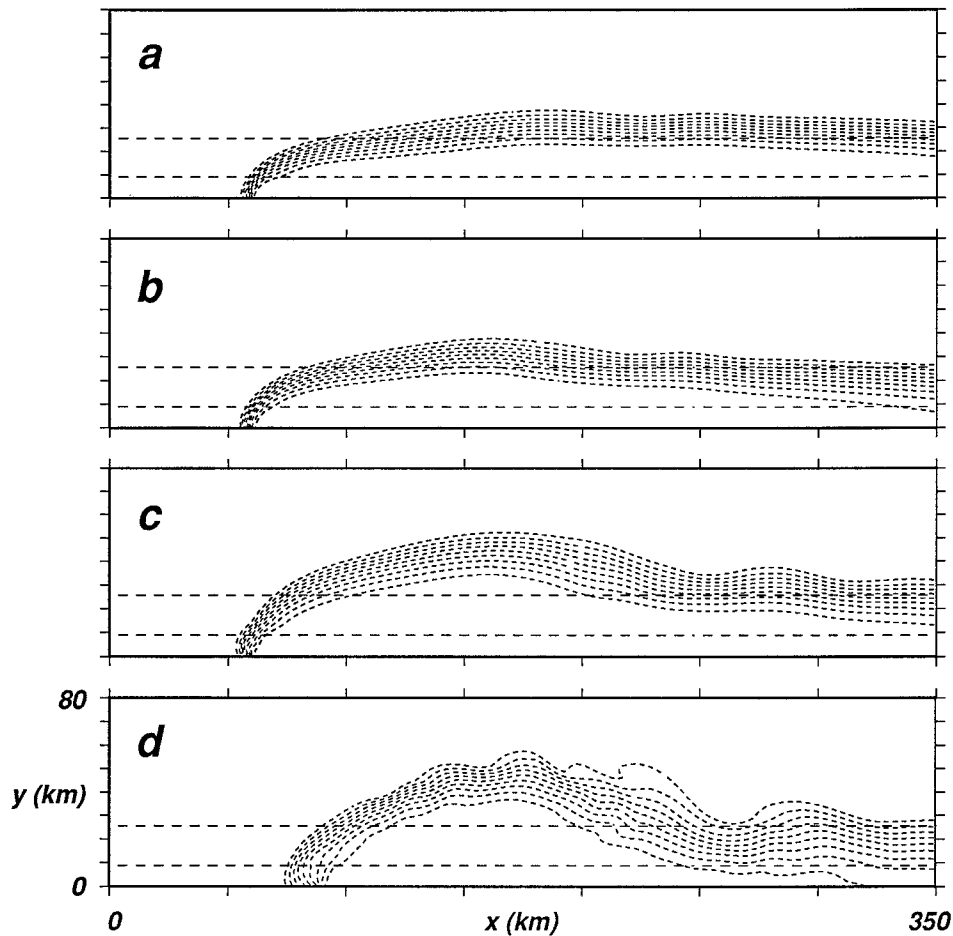
FIG. 13. As in Fig. 12 but plan views of density anomaly at the surface. Contours are $0.1\rho_i$ to $0.9\rho_i$ by $0.1\rho_i$ kg m^{-3} in each panel. The straight dashed lines are the 50-m and 100-m isobaths.

1) represents a smaller transport with greater density difference (approximately 50%–60% of the total transport toward the Labrador Shelf). The second (Labrador 2) is probably more realistic, with a greater transport of slightly less buoyant water (see Table 2).

In both cases, the theory predicts a bottom-advected plume over the Labrador Shelf. For Labrador 1, the equilibrium isobath, $h_b = 120$ m, is located 30–40 km offshore at Saglek Bank, while y_s is only 27 km. Labrador 2 is more consistent with the observations predicting $h_b = 165$ m. In fact, the base of the observed frontal zone occupies a depth of about 200 m [e.g., Fig. 15 of Lazier and Wright (1993), or Fig. 2 of Narayanan and Webster (1988)]. Considering the uncertainties in the parameter estimates, these results again support the theory.

The next example is the Connecticut River during conditions of high runoff described by Garvine (1974). This plume is the purest example of a surface-advected plume that we could find (Table 2). We consider specific observations obtained on 13 April 1973 (Garvine 1974). We choose $L = 1.5$ km and $v_i = 0.34$ m s^{-1} (which

follows from the discharge value of 1020 m^3 s^{-1} observed on that particular day). The average density difference between discharge and ambient flow is 9 kg m^{-3}, and $h_0 = 2$ m, both based on Fig. 5 of Garvine (1974). With these values, our theory predicts a pure surface-advected plume with $y_s = 20.1$ km and $h_b = 1.5$ m. Again, the prediction of plume type is correct. The estimate of y_s is somewhat greater than observed, but this is not surprising considering that the theory neglects the strong winds and tidal forcing known to affect the Connecticut River plume.

Another good example of a surface-advected plume is produced by the Hudson River runoff (Table 2). In this case, the river discharge reaches the ocean shelf through an estuary resulting in an effective increase in inflow transport and a decrease in density difference. Doyle and Wilson (1978) provide velocity and density sections at the mouth (between Rockaway Point and Sandy Hook) during summer. We choose $L = 7$ km (there is a mean flow into the estuary along the northern coast), $h_0 = 10$ m, an inflow density anomaly of $\rho_i = 2$ kg m^{-3} and a typical inflow velocity of $v_i = 0.1$ m
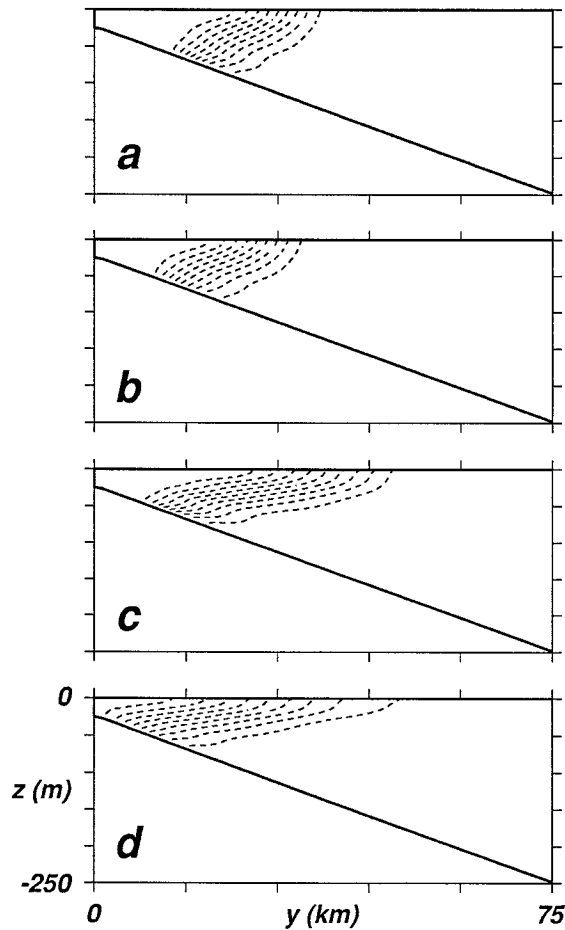
FIG. 14. Cross-shelf sections of density anomaly for the cases shown in Figs. 12 and 13. (a) Run 6, (b) run 7, (c) run 8, and (d) run 9. (a)–(c) are at $x = 200$ km. (d) is at $x = 230$ km. Contours are $0.1\rho_i$ to $0.9\rho_i$ by $0.1\rho_i$ kg m^{-3} in each panel.

s^{-1}. The predicted equilibrium depth h_b is 8.2 m, which is less than h_0, and $y_s = 20.1$ km, indicating a pure surface-advected plume. Observations of this plume in August 1976 (Bowman 1978) show that the plume is thin (about 5 m deep) and extends from the mouth seaward for 10–25 km depending on prevailing winds, both features being consistent with our theory.

To the south along the eastern U.S. coast is Delaware Bay (the estuary of the Delaware River). Observations reported by Münchow and Garvine (1993) show that this plume has the structure of a bottom-advected plume throughout most of the year. However, during spring the freshwater runoff exceeds the average value by an order of magnitude, resulting in an intermediate or perhaps a surface-advected plume. Therefore, for the Delaware plume, we consider three different values of inflow density anomaly (Table 2): 0.5 kg m^{-3}, typical for most of the year (Fig. 3a of Münchow and Garvine 1993); 1 kg m^{-3}, which represents higher runoff from the Delaware River typically observed from April to June (Fig. 3b of Münchow and Garvine 1993; see also Wong and Münchow 1995); and 3.5 kg m^{-3}, which represents the peak value of the Delaware River discharge (e.g., in mid-May 1989; Münchow and Garvine 1993). For the first two cases, we choose $v_i = 0.1$ m s^{-1}, while for case 3 we choose $v_i = 0.15$ m s^{-1}. For all three cases, we choose $L = 10$ km and $h_0 = 15$ m, remembering that there is a mean flow into the estuary from the ocean at the bottom and along the northern boundary. For the first case (Delaware 1), theory predicts $y_s = 12.8$ km and $h_b = 23.8$ m. The 25-m isobath lies about 20–25 km offshore, so the discharge should form a bottom-advected plume. Both Figs. 9 and 10 from Münchow and Garvine (1993) confirm this structure. The second case (Delaware 2) produces $y_s = 18$ km and $h_b = 16.8$ m. This shallower isobath is located roughly 15–20 km offshore, depending on the particular choice of the depth profile. Thus, both scales are comparable, so a bottom-advected plume should form again. Observations slightly downstream from the mouth show that the plume extends 15–20 km seaward at the surface, and it appears to be confined to about the 18-m isobath (sections C and D in Fig. 9 of Wong and Münchow 1995). Finally, the third case (Delaware 3) predicts a surface-advected plume with $y_s = 33.5$ km and $h_b = 11.0$ m. Figure 10 of Münchow and Garvine (1993) supports this prediction at a time when wind forcing was weak, so the plume dynamics were not too contaminated by another process. The frontal zone meets the bottom between 12 and 17 m, and extends offshore more than 30 km.

The buoyant discharge originating from Chesapeake

TABLE 2. Parameters used for the observational examples discussed in section 4. Variables are defined in the text. Units are kilometers for L and y_s; meters per second for v_i; meters for h_0 and h_b; kilograms per cubic meter for ρ_i and ρ_0; s^{-1} for f.

Example	L	v_i	h_0	ρ_i	ρ_0	$f(\times 10^{-4})$	y_s	h_b
Niagara 1	1.5	0.4	10	0.5	1000.0	0.99	12.2	15.6
Niagara 2	1.5	0.4	10	0.9	1000.0	0.99	14.8	11.6
Labrador 1	50	0.15	70	1.0	1026.5	1.30	26.8	119.6
Labrador 2	50	0.15	100	0.75	1026.5	1.30	27.7	165.0
Connecticut	1.5	0.34	2	9.0	1020.0	0.93	20.1	1.5
Hudson River	7	0.1	10	2.0	1021.0	0.93	20.1	8.2
Delaware 1	10	0.1	15	0.5	1025.0	0.90	12.8	23.8
Delaware 2	10	0.1	15	1.0	1025.0	0.90	18.0	16.8
Delaware 3	10	0.15	15	3.5	1025.0	0.90	33.5	11.0
Chesapeake	15	0.1	10	3.0	1020.0	0.87	26.3	9.5

Bay forms a surface-advected plume, which is discussed in detail by Boicourt (1973). Average values of the inflow parameters, typical for summer, are listed in Table 2. The predicted equilibrium depth is $h_b = 9.5$ m, slightly less than the buoyant inflow depth of $h_0 = 10$ m, so the plume should be surface-advected with an offshore extent of $y_s = 26.3$ km. Cross-shelf sections south of Cape Henry (i.e., downstream from the mouth), obtained in the summers of 1971 and 1972, are in good agreement with these estimates. For instance, Boicourt's (1973) Fig. 5.34 shows a salinity section at 36°40′ with the plume extending 20–30 km offshore while occupying the upper 7–9 m of the water column, consistent with the theory.

5. Summary and discussion

We have used a simple theory to derive two lengths associated with a buoyant discharge onto a continental shelf subject to rotational effects. The equilibrium depth h_b represents the depth to which bottom boundary layer processes can move the buoyant discharge. The offshore distance y_s represents the extent to which a plume may spread at the surface, being unaffected by contact with the bottom. These scales are based solely on the properties of the buoyant inflow at the source and the inflow geometry. They do not require knowledge of the ambient shelf circulation or estimation of any frictional or mixing properties, which are generally poorly known. Based of these lengths, we identify three possible types of plumes that may form in the absence of ambient shelf circulation effects.

1) If the offshore distance to the h_b isobath (y_b) is greater than y_s, then a *bottom-advected plume* will form (Fig. 1), characterized by a surface-to-bottom front (separating the buoyant water from the ambient shelf water) which remains attached to the bottom along the h_b isobath.
2) If the predicted h_b isobath is shallower than the depth of the inflow, then bottom effects are negligible, and a shallow *surface-advected plume* spreads radially outward from the source (Fig. 2) to an offshore distance y_s. Interestingly, a surface-advected plume spreads offshore a *minimum* of more than four Rossby radii (based on the inflow), a result which is consistent with this and other studies but has apparently not been previously reported.
3) If the predicted h_b isobath is deeper than the inflow depth, but the h_b isobath is closer to the coast than y_s, then an intermediate plume will form, with both surface-advected and bottom-advected plume features. The inflow near the surface will form an anticyclone extending seaward, while the inflow near the bottom will form a bottom-advected plume structure extending downstream. The frontal zone will attach to the bottom at the h_b isobath, but the upper part of the front will extend farther seaward to y_s.

A bottom-advected plume is typically established when the buoyant inflow has a large transport and/or a small density difference from the ambient shelf water. There is a critical inflow density anomaly for every basin geometry above which the surface-advected plume becomes dominant, no matter how strong the inflow velocity may be, and an intermediate or surface-advected plume develops. Thus, direct river discharge onto the shelf always tends to form a surface-advected plume. Similarly, surface-advected plumes are more likely at lower latitudes where the relative effects of stratification are stronger owing to the reduced Coriolis parameter.

We have applied our theory to both numerical modeling results and field observations. In all cases considered, the prediction of the plume type was correct. The actual scales were also in fairly good agreement with the estimates. Therefore, we believe these simple ideas may provide a useful theoretical framework for understanding the behavior of a wide variety of buoyant coastal discharges.

Of course, we have made many simplifications in deriving the theory in section 2. For example, the scale of the plume must be large enough for rotational effects to be important. That is, (2) and (7) are not sensible in the limit $f \to 0$. We have also ignored lateral diffusion and mixing, while implicitly considering vertical mixing in the bottom-advected plume. In the numerical model calculations, lateral mixing is weak, at least one order of magnitude smaller than the other terms in the momentum and density balances. On the other hand, even small lateral mixing can alter the plume structure when allowed to operate for extended periods of time, as done in section 3. As a result, the scales y_s and y_b (or h_b) tend to correspond to the shoreward edge of the frontal zone at the later stages of the numerical calculations. We do not expect the inclusion of larger lateral mixing to substantially alter the comparison of the plume scales because both plume types would be equally subject to the increased mixing.

In the ocean, shelf circulation consumes buoyant inflows much more effectively than in our calculations, that is, most plumes have a limited alongshelf extent. Also, real buoyant inflows change in time, so the actual period of adjustment is shorter than in the model. As a result, y_s and y_b are more appropriately applied to the center of the frontal zone in observations. Due to the large variety of natural topographies, it is better to apply h_b directly to the actual depth profile rather then trying to approximate an average bottom slope for the analytical expression for y_b.

We have not considered explicitly the influence of external forcing (e.g., wind or tidal) on plume dynamics. In fact, such forcing may modify the shape of the plume, its offshore extent, the rate of mixing, etc. However, the influence of external forcing sometimes appears implicitly through the parameters of the buoyant inflow. For example, stronger tidal forcing may produce stron-

ger currents through the estuary mouth, which lead to enhanced mixing of the river discharge. As a result, the buoyant inflow may have a greater transport and smaller density anomaly that ultimately increases h_b. Weaker forcing implies weaker mixing in the estuary, resulting in less transport of more buoyant water onto the shelf.

We also recognize that buoyant inflows are not always isolated. It would be interesting to extend this simple theory to cases where there are multiple sources of buoyancy along a coast. Some examples are the Gulf of Alaska and the South Atlantic Bight. For these cases, we would probably need to introduce more realistic lateral exchange of the plume with the ambient ocean. This remains for the future.

REFERENCES

Boicourt, W. C., 1973: The circulation of water on the continental shelf from Chesapeake Bay to Cape Hatteras. Ph.D. dissertation, The Johns Hopkins University, 183 pp.

Bowman, M. J., 1978: Spreading and mixing of the Hudson River effluent into the New York Bight. *Hydrodynamics of Estuaries and Fjords,* J. C. J. Nihoul, Ed., Elsevier, 373–386.

Chao, S.-Y., 1988: River-forced estuarine plumes. *J. Phys. Oceanogr.,* **18,** 72–88.

——, and W. C. Boicourt, 1986: Onset of estuarine plumes. *J. Phys. Oceanogr.,* **16,** 2137–2149.

Chapman, D. C., and S. J. Lentz, 1994: Trapping of a coastal density front by the bottom boundary layer. *J. Phys. Oceanogr.,* **24,** 1464–1479.

Collings, I. L., and R. Grimshaw, 1980: The effect of topography on the stability of a barotropic coastal current. *Dyn. Atmos. Oceans,* **5,** 83–106.

Csanady, G. T., 1978: The arrested topographic wave. *J. Phys. Oceanogr.,* **8,** 47–62.

——, 1984: Circulation induced by river inflow in well mixed water over a sloping continental shelf. *J. Phys. Oceanogr.,* **14,** 1703–1711.

Doyle, B. E., and R. E. Wilson, 1978: Lateral dynamic balance in the Sandy Hook to Rockaway Point transect. *Estuarine Coastal Mar. Sci.,* **6,** 165–174.

Drinkwater, K. F., 1988: On the mean and tidal currents in Hudson Strait. *Atmos.–Ocean,* **26,** 252–266.

Garvine, R. W., 1974: Physical features of the Connecticut River outflow during high discharge. *J. Geophys. Res.,* **79,** 831–846.

——, 1987: Estuary plumes and fronts in shelf waters: A layer model. *J. Phys. Oceanogr.,* **17,** 1877–1896.

——, 1996: Buoyant discharge on the inner continental shelf: A frontal model. *J. Mar. Res.,* **54,** 1–33.

Gill, A. E., 1982. *Atmosphere–Ocean Dynamics.* Academic Press, 662 pp.

Haidvogel, D. B., J. L. Wilkin, and R. Young, 1991: A semi-spectral primitive equation ocean circulation model using vertical sigma and orthogonal curvilinear horizontal coordinates. *J. Comput. Phys.,* **94,** 151–185.

Kourafalou, V. K., L.-Y. Oey, J. D. Wang, and T. N. Lee, 1996: The fate of river discharge on the continental shelf. 1. Modeling the river plume and the inner shelf coastal current. *J. Geophys. Res.,* **101,** 3415–3434.

Lazier, J. R. N., and D. G. Wright, 1993: Annual velocity variations in the Labrador Current. *J. Phys. Oceanogr.,* **23,** 659–678.

Masse, A. K., and C. R. Murthy, 1992: Analysis of the Niagara River plume dynamics. *J. Geophys. Res.,* **97,** 2403–2420.

Münchow, A., and R. W. Garvine, 1993: Dynamical properties of a buoyancy-driven coastal current. *J. Geophys. Res.,* **98,** 20 063–20 077.

Narayanan, S., and I. Webster, 1988: Coastally trapped waves in the presence of a shelf edge density front. *J. Geophys. Res.,* **93,** 14 025–14 031.

O'Donnell, J., 1990: The formation and fate of a river plume: A numerical model. *J. Phys. Oceanogr.,* **20,** 551–569.

Oey, L.-Y., and G. L. Mellor, 1993: Subtidal variability of estuarine outflow, plume, and coastal current: A model study. *J. Phys. Oceanogr.,* **23,** 164–171.

Wong, K.-C., and A. Münchow, 1995: Buoyancy forced interaction between estuary and inner shelf: Observation. *Contin. Shelf Res.,* **15,** 59–88.

Wright, D. G., 1989: On the alongshelf evolution of an idealized density front. *J. Phys. Oceanogr.,* **19,** 532–541.